Fractal-like hierarchical organization of bone begins at the nanoscale

Natalie Reznikov[b], Matthew Bilton[a,c], Leonardo Lari[a,d], Molly M. Stevens [b,*], Roland Kröger[a,*]

[a)]Department of Physics, University of York, Heslington, York, United Kingdom

[b)]Department of Materials, Department of Bioengineering and Institute for Biomedical Engineering, Faculty of Engineering, Imperial College London, United Kingdom

[c)]4D LABS, Simon Fraser University, Burnaby, British Columbia, Canada

[d)]JEOL York Nanocentre, Science Park, York, United Kingdom

[*]Corresponding authors: roland.kroger@york.ac.uk, m.stevens@imperial.ac.uk

Bone is a hierarchical material and its exceptional bulk properties depend on the assembly of its components at the nanometer level. The organization and relationship of mineral and collagen in bone has long been a matter of dispute. Using 3D imaging from electron tomography, and high-resolution 2D electron microscopy, we demonstrate that bone mineral is hierarchically assembled from the nanoscale: needle-shaped mineral units merge laterally to form platelets, and these are further organized into stacks of multiple roughly parallel platelets. These stacks coalesce into larger entities significantly exceeding the lateral dimensions of the collagen fibrils, thus contributing to a continuous cross-fibrillar mineralization pattern. From this, we present a hierarchical structural model of the mineral phase which reconciles previous contradictory views, and further explains some of the remarkable properties of bone.

Bone is a most impressive natural material that combines properties which are usually mutually exclusive – stiffness (for support and leverage) and toughness (for protection and resisting impacts). In bone, stiffness coexists with toughness by virtue of bone's hierarchical organization, that means smaller structural units form larger structural units, which in turn are structured themselves in this manner into higher order units.

In light of previous studies of bone structure, analyzed at different scales, an informative and intriguing picture emerges. At the macroscopic level, most bones incorporate a helical motif in their anatomical shape. For example, this helical motif can be recognized by the twisting of grooves and tuberosities along the shaft of the humerus, by the curvature of the clavicle, or by the course of a rib with respect to the body axis (*1*). These twisted or helical morphologies are easy to identify on robust bones that are well adapted to loading. At the millimeter level, multiple Haversian canals traverse compact bone roughly aligned with the longitudinal axis of the shaft. In fact, they form helical arrays where each canal and its associated osteon lie along a screw-shaped trajectory with a roughly constant small pitch; this is presumably an adaptation to loading (*2*). At the micrometer level, the helical secondary osteons themselves are formed of concentric lamellae of mineralized collagen fibrils. These fibrillar arrays are inclined with respect to the

central Haversian canal at an average angle of approximately 30°, thus forming an assembly of nested coils with alternating pitches (*3*). A single lamella in three dimensions often appears as a layer of bundles each being 2-3 μm in diameter, in which mineralized collagen fibrils twist around the bundle axis, like filaments of a rope twist around its axis with a shallow pitch (*4*). At the nanometer level, the helical theme continues as quasi-hexagonal packing of triple helices of collagen into a fibril (*5*). Each collagen triple helix itself is a supercoil of single α-chain helices (*6*). This abridged overview of independently described helical motifs in bone highlights remarkable self-affinity of structure across 9 or 10 orders of magnitude (in mathematical terms, self-affinity is a less restricted notion than self-similarity). Indeed, in Nature, it is not uncommon to observe self-affine patterns (also called fractal-like), in which a part of the structure resembles larger entities and/or the whole structure (*7*). Many natural self-affine patterns are helical or spiral (*8*).

Existing evidence describing bone structural hierarchy states that below the sub-micrometer level, the helical pattern pertains only to the collagen component. For bone mineral alone, the paradigm of self-affinity is not obvious. Details of the architecture of both the organic and inorganic constituents of bone have become available with the advancement of X-ray diffraction and electron microscopy methodologies. The mineral of bone – carbonate-substituted hydroxyapatite – has to occupy a preformed, osmotically crowded, covalently crosslinked organic niche. Prior to mineralization, the organic phase of bone is already assembled and is capable of the fine regulation of crystal nucleation and growth (*9*). Bone mineral is nano- and polycrystalline with a substantial degree of disorder and a significant amount of substitution (*10-12*). These features lead to inherent difficulties in the interpretation of crystallographic data. Furthermore, X-ray based methods require relatively large sampling volumes where the crystallographic observations are averaged and often isolated from their immediate structural context. Another characterization challenge is that bone apatite is associated with disordered or amorphous phases (*13*). These mineral phases, such as octacalcium phosphate (*14*) and amorphous calcium phosphate (*15*), are stabilized by noncollagenous proteins (*16*), citrate ions (*17*), and by a rigid hydration shell (*18*). Therefore, the ripening of the crystals is inhibited especially where they interface with organic moieties (*19*). As a result, multiple mineral phases are thought to coexist in bone (*20, 21*), which also complicates the interpretation of crystallographic studies. The complex structure of skeletal mineral often makes it difficult to prepare samples for electron microscopy imaging without causing specimen-preparation artifacts such as disintegration, dehydration and/or destabilization of metastable mineral phases (*22*). Finally, the 3D structure of bone mineral, and thus the hierarchical structure, cannot be reconstructed exclusively based on 2D information. For these reasons, it is not surprising that diverse, sometimes conflicting views have evolved regarding bone mineral morphology and its relationships with the organic extracellular matrix. A number of predominantly electron microscopy-based studies identify the bone mineral building blocks as being acicular (needle-shaped) nanocrystals with diameters between 3 and 10 nm and a length of several hundred nanometers (*23-25*), or as platelets with a variety of dimensions ranging from 5 × 20 × 40 nm

(*26*) to 100 nm in the largest dimension (*27*). Furthermore, there is apparent disagreement as to whether the mineral phase is growing in an intra- or extrafibrillar fashion (*28*), a matter of great significance for the structural integrity of bone. Based on this information, there is no consensus on the fine details of bone mineral morphology and organization. Besides explaining its unique mechanical properties, a clearer understanding of the mineral-organic interface in the context of bone hierarchical structure will provide insight on skeletal pathologies, growth and development defects, diagenesis (postmortem modification over time) as well as the metabolic role of bone as an ion reservoir. The organization and relationships between mineral and the organic extracellular matrix are important in such diverse fields as osteology, endocrinology, forensic medicine and archaeology, and this information may additionally inspire the design of novel composite materials.

Our work aims to evaluate the mineral phase of bone in three dimensions, within its immediate structural framework, in such a way that preparation artifacts are minimized and the hierarchical context of bone structure is taken into consideration. Using advanced preparation methodology and high-resolution electron microscopy, we explain how earlier conflicting models can be reconciled and advanced by the findings presented here.

Two-dimensional projections of the apatite mineral phase

Lamellar bone is the most common type of bone in a mature skeleton. Mineralized collagen fibrils are ordered and tightly packed within a single lamella (*29*). On the micron scale, mineralized collagen fibrils can be considered to be roughly co-aligned, whereas their orientation changes more-or-less abruptly at the boundaries between adjacent lamellae.

By aligning an FIB-milled, electron-transparent specimen perpendicular to the lamellar boundaries, one can expect to observe the collagen fibrils with respect to the image plane in a wide range of orientations from edge-on views to in-plane views (*29*). We assumed that using such specimen geometry, nearly in-plane and nearly edge-on arrays of mineralized collagen fibrils could be observed in the resulting cross-sections (see Fig S1). Interestingly, three distinct motifs of mineral organization were identified as shown in Fig. 1.

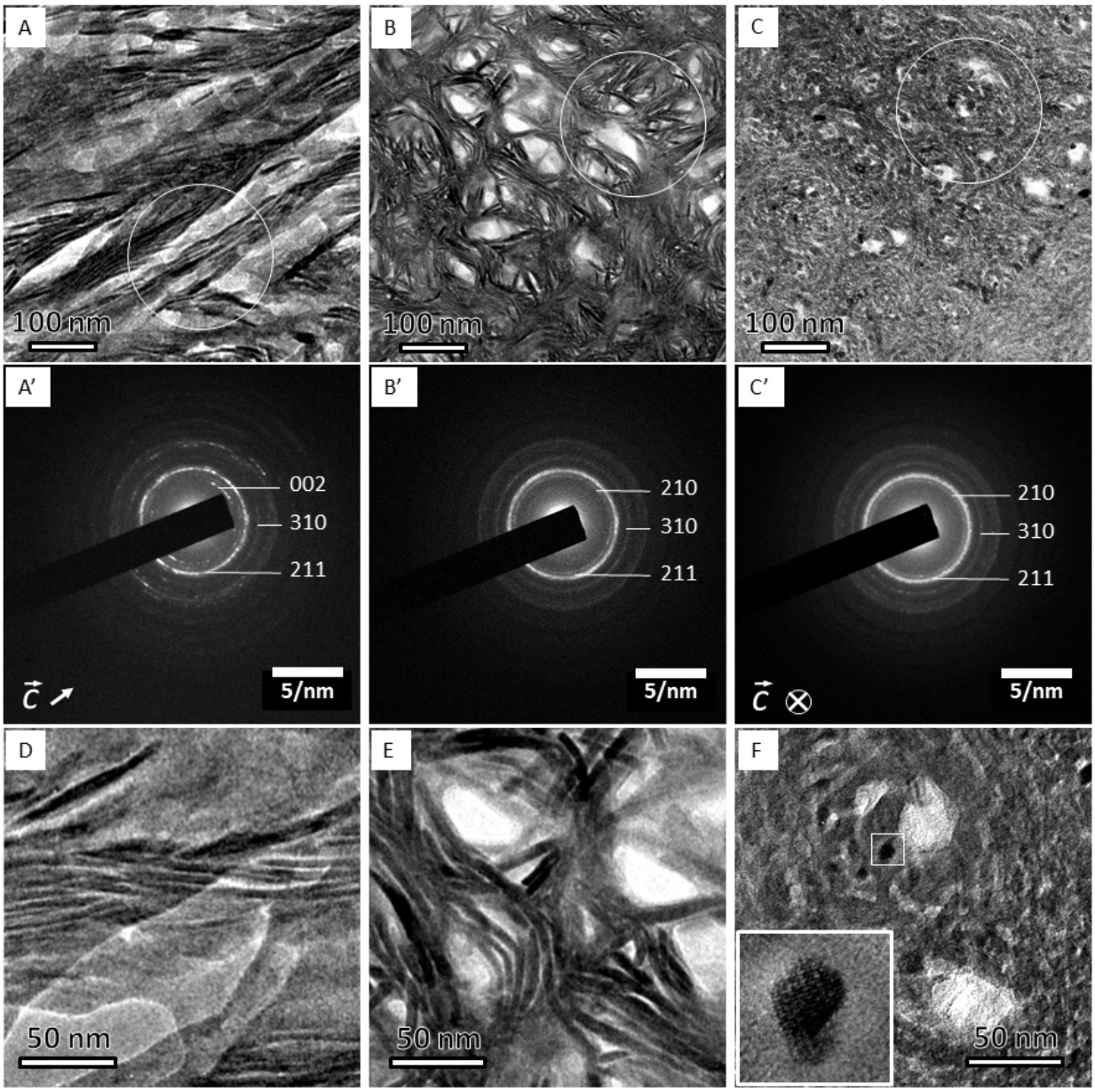

Figure 1: Three projections of bone structure as observed by TEM and corresponding electron diffraction patterns. (A) The filamentous pattern shows curved, more than 100 nm-long crystals. (A') diffraction pattern from (A) shows well-defined (002) plane-related reflections, which are oriented in the direction of the elongated crystals. (B) The lacey pattern comprises groups of parallel, slightly bent crystals surrounding electron-transparent voids. The absence of the (002) plane-related reflections in (B') indicates that the crystals' *c*-axes are oriented out of plane. (C) Nested rosettes, a previously unknown pattern, shows crystals of about 5 nm in size arranged into left-handed helices. (C') Corresponding diffraction pattern with (002) plane-related reflections being absent, similar to that in (B'). Higher

magnification of the same motifs, D-F. (D) The filamentous motif. (E) The lacey motif. (F) The rosette motif. Note a nearly hexagonal outline of the dark crystallite in (F); the inset shows a high-resolution transmission electron microscope (HRTEM) view of the area indicated by the small white square, and the white circles in A, B and C indicate the areas from which the selected-area electron diffraction patterns A', B' and C' were recorded.

Of the three revealed motifs of nanoscale bone organization, the first, in-plane motif (Fig. 1A) contains extended quasi-linear elements, referred to hereafter in the text as the filamentous motif. The 67 nm D-periodicity of collagen fibrils can be followed in this orientation, confirming that the fibrils are roughly aligned with the image plane. The filamentous mineral particles are roughly co-oriented with the D-periodicity (at an angular range of approximately ± 20°) and therefore are aligned with the long axes of the collagen fibrils. However, the length of the mineral particles usually exceeds 67 nm, suggesting that they are not confined to a single period of the collagen fibril. Similar filamentous motifs have been reported previously (*30-32*). The second, 'lacey' pattern (Fig. 1B) incorporates groups of concentrically curved, thin mineral particles surrounding irregular voids of 30-50 nm in diameter. The third pattern of mineral particle arrangement is relatively dense, and comprises left-handed rosettes with lateral crystal sizes between 5 nm and 10 nm. These rosettes of edge-on imaged particles are assembled in a quasi-closely packed pattern when the outlines of entire rosettes are considered.

Selected-area electron diffraction (SAED) patterns obtained from all three motifs are presented in Fig. 1 (A' – C'). All SAED patterns indicate polycrystallinity and are somewhat spotty in nature attributable to the limited number of refracting crystals in the analyzed volumes (SAED area diameter: 250 nm). The azimuthal intensity distribution is therefore not homogeneous, yet the radial intensity distribution clearly indicates the presence of apatite-related reflections and allows for the extraction of important crystallographic information. The filamentous motif shows a pair of arcs corresponding to the (002) plane-related reflection. The arc axis with respect to the center of the diffraction patterns is aligned with the texture of the filamentous motif, and the angular dispersion of both is in agreement. The systematic absence of (002) plane-related reflections in Figs. 1B' and 1C' indicates that the crystallographic *c*-axes are significantly tilted out of the plane of view, as would be expected if the mineralized collagen fibrils are out-of-plane.

Higher magnification images of the three motifs are presented in Figs. 1D-F. The crystallographic planes of mineral particles can be traced to about 5 nm laterally (in thickness, such as in Fig. 1F and to some extent in Fig. 1E), and to more than 100 nm longitudinally (see e.g. Fig. 1D). Interestingly, the individual crystals are not exactly straight in Fig. 1A and D, but rather display bending with curvature radii varying between 50 and 150 nm.

As shown in Fig. 1 (B and C), we found two motifs when the mineralized fibrils are observed in cross-section. The observed lacey motif has been previously reported (*12, 28-31, 33, 34*),

whereas the second rosette motif previously has not been described. Each of the rosettes is a chain of hexagonally facetted crystals with clearly visible lattice fringes when imaged by HRTEM (Fig. 1F). Analysis of the lattice fringes shows that the long *c*-axes of the crystals are approximately parallel to the zone axis (see Figs. 1F and S2). As a result the *c*-axis orientation could be approximately indicated in the SAED pattern in Fig. 1A' as in-plane and in 1C'as out-of-plane, whereas the corresponding *a*- and *b*-axes are randomly distributed as confirmed by the SAED patterns.

Interestingly, the lateral extension of the rosettes in the motif shown in Fig. 1C is between 100 and 120 nm, which is consistent with the diameter of collagen fibrils in bone. Furthermore, their close-packing arrangement is reminiscent of the quasi-hexagonal packing of bone collagen fibrils (*5, 35*). These observations raise the question as to how the same, presumably edge-on projection can generate two distinct structural patterns.

Three-dimensional morphology of bone mineral

Tomographic tilt series were acquired from five FIB-milled sections of which we present the results for two sections that at the 0°-tilt angle revealed *i*) a domain containing the filamentous and the lacey motifs simultaneously, and *ii*) a domain containing exclusively the lacey motif. The lateral resolution of tomographic images exceeds the z-resolution because the z-axis dimension is reconstructed from tilted projections of an electron-transparent specimen. In tilted projections, the electron beam travels through a larger thickness compared to the 0°-tilt projection. For this reason it was important to reconstruct 3D images from specimen areas containing in-plane and out-of-plane mineralized collagen fibrils. The resulting reconstructions were rendered and are shown in Figs. 2 and 3. *Z*-contrast imaging allows for a clear distinction of the mineral phase in the context of the organic matrix. However, the mass density variation attributable to the sequence of gap and overlap regions makes it also possible to observe the collagen D-periodicity simultaneously with the mineral phase, without the need for any staining agent. We collected tilt series of STEM images at tilt-angle increments of 2° through a tilt range of ± 70°. The tilt series were reconstructed into 3D stacks (tomograms) using a filtered back-projection algorithm applying the IMOD 4.9.0 software (http://bio3d.colorado.edu/imod/ (*36*)). The volume-rendered tomograms are presented in supplemental videos SV1 and SV2. The three-dimensional reconstructed volumes show the in-plane filamentous motif and/or the out-of-plane lacey motif. In the 3D view, both appear as assemblies of irregularly shaped, opaque and elongated mineral particles. Crystals in the filamentous motif are roughly aligned with the collagen fibrils that are identified by their D-periodicity (Fig. 2A); the lacey motifs display lens-shaped voids of 20-50 nm in diameter, the size and distribution of which within the imaged volume are far less than that of collagen fibrils observed in 3D studies of demineralized bone (*29, 37*).

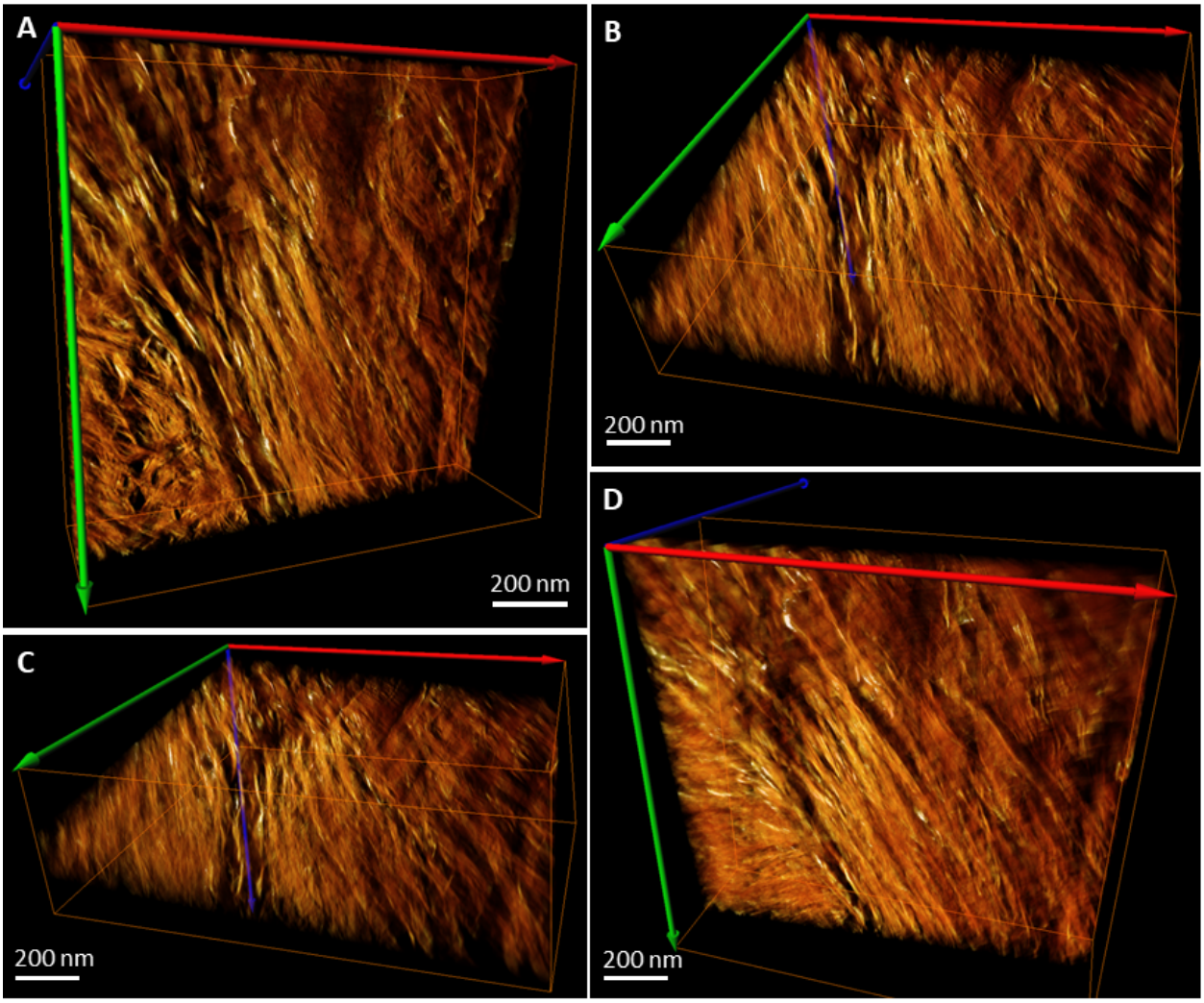

Figure 2: Reconstructed and rendered STEM tomogram in different projections of an FIB-milled specimen of mature human lamellar bone. Panel (A) shows mostly the filamentous pattern with a fragment of the lacey pattern in the bottom left corner – these patterns originate from two adjacent lamellae. Panel (B) shows the same volume slightly tilted around the horizontal axis. Panel (C) shows the same volume (A) tilted approximately 50-60° around the horizontal axis. Panel (D) shows the same volume (A) tilted approximately -30° around the horizontal axis. Note the angular offset of approximately 60° between the crystallites of the neighboring motifs apparent in (C). Colored arrows indicate the axes of the reconstructed 3D-volume orientation in space.

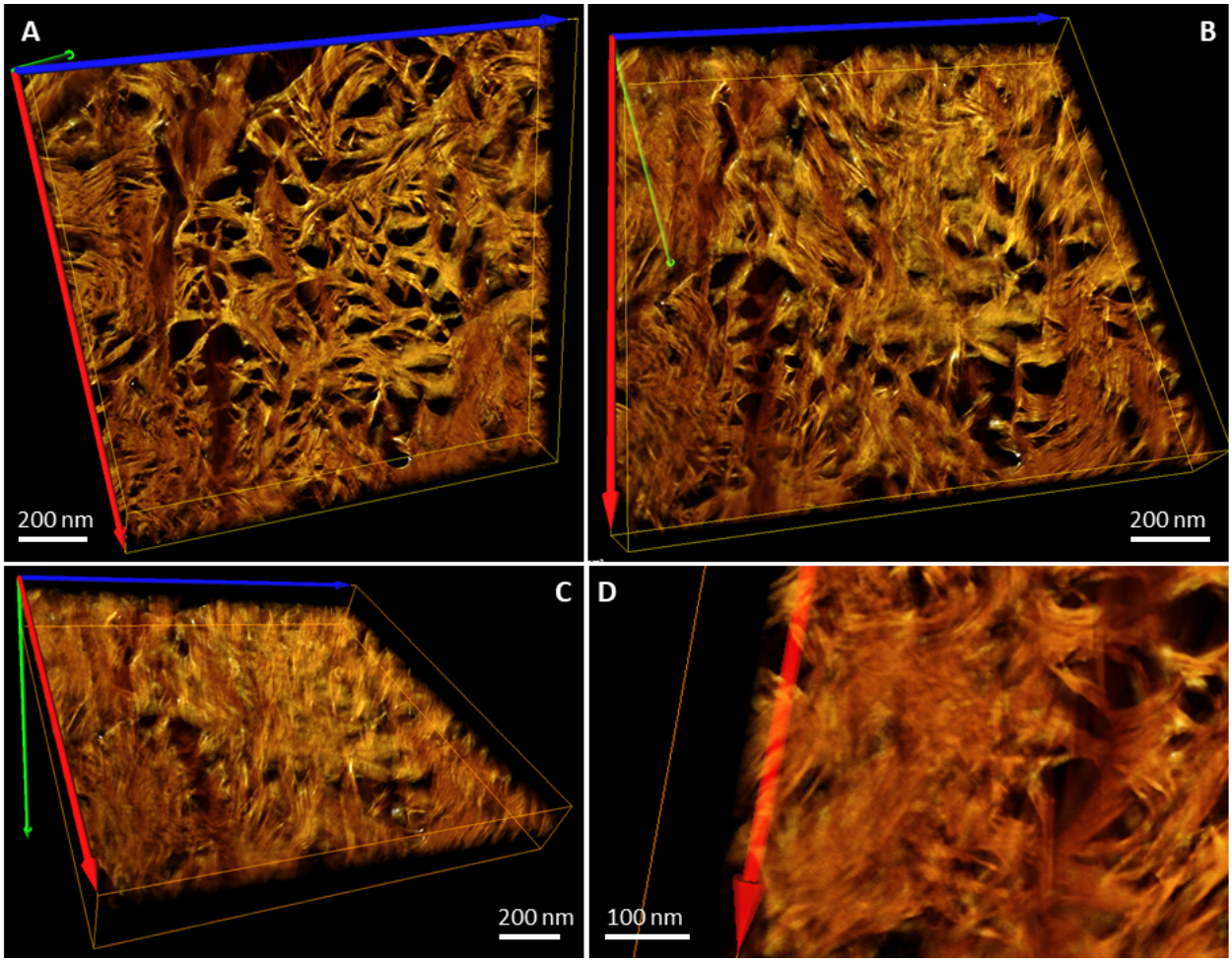

Figure 3: Reconstructed and rendered STEM tomogram in different projections of an FIB-milled specimen of mature human lamellar bone. Tomogram of a sample with the lacey motif at the 0°-tilt angle. Panels A, B and C show the same volume viewed vertically (A), tilted approximately 30° around the horizontal axis (B), and tilted approximately 60° around the horizontal axis (C). Note that in the right top corner of (C) the faint D-periodicity of collagen can be detected. Panel (D) shows a fragment of the same sample in such an orientation that acicular projections of the crystallites appear, resembling the rosette pattern in Fig. 1C. Colored arrows indicate the axes of the reconstructed 3D-volume orientation in space.

We took advantage of finding two adjacent motifs (lacey and filamentous) at the boundary of two bone lamellae in the same tomogram, *i.e.* they have the same thickness and are imaged under identical conditions, and we performed virtual re-slicing of digitally isolated filamentous and lacey areas. This allowed us to examine whether these two motifs are projections of morphologically identical crystalline assemblies. Two cubic volumes each of 100 nm size were cropped from each area and globally labeled applying a White TopHat algorithm (*38*) – a

function used for en masse extraction of small features in digital image processing (Avizo 9.2, FEI, USA). The resulting binary cubic images were digitally resliced at 90°, so that the original in-plane area would be viewed edge-on, and vice versa. Subsequently, all images comprising the resliced stack were overlaid into a single image (a digital projection) using average pixel values, and the brightness was adjusted. The resulting original and reciprocal projections of in-plane and out-of-plane arrays are presented in Fig. 4, demonstrating that essentially the lacey and filamentous motifs are different projections of the same 3D arrangement.

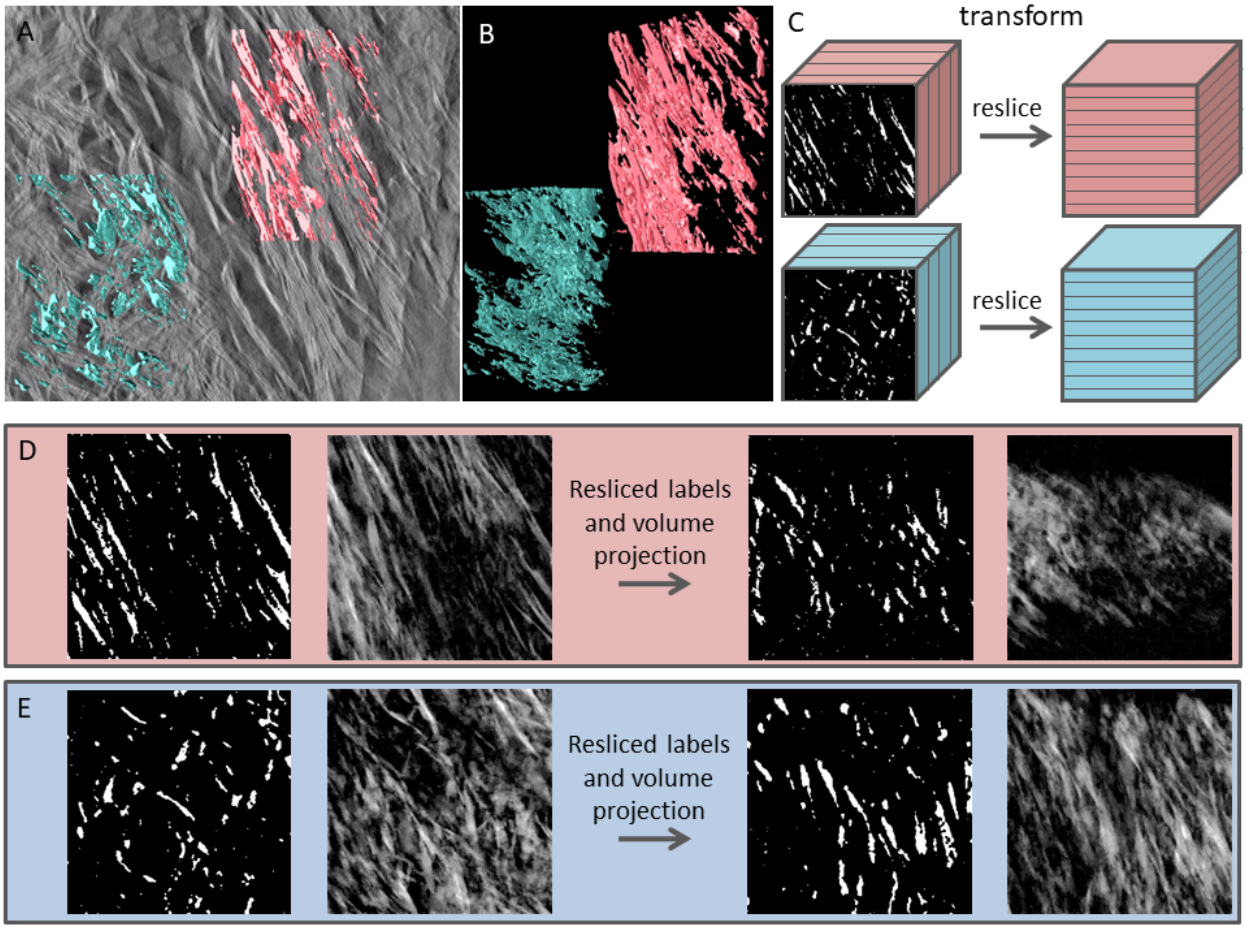

Figure 4: Labeling algorithm and comparison of the lacey and filamentous patterns in bone in reciprocally oriented projections. (A) Tomogram slice with superimposed labels of the lacey (blue) and filamentous (pink) patterns. (B) Labeled volumes show extensively aggregated and coalesced elongated entities of variable size and irregular shape. (C) Volumes cropped to an identical size in all 3 dimensions are transformed in such a way that former XY-planes now are XZ-planes, *i.e.* the in-plane labels are viewed in the out-of-plane orientation, and vice versa. (D) Digital manipulation of the filamentous label field (from left to right): original labels in a cubic stack are averaged in terms of pixel value to form a pseudo-2D image, which is similar to the corresponding area in (A). The resliced label field

stack is averaged in terms of pixel value to form a pseudo-2D image in an orthogonal direction. (E) Digital manipulation of the lacey label field follows the same sequence of steps. Note the similarity of the resliced projected filamentous label field to the original lacey motif, and vice versa.

Besides demonstrating that lacey and filamentous motifs are different projections of identical structures, Fig. 4 also shows that the TopHat-labeling algorithm results in a reliable and feature-retaining segmentation of bone mineral. We used 3D-rendering of individual mineral particle labels to study their morphology while avoiding the masking effect of the neighboring, coalescing labels. Separate mineral particles and their aggregates showing the least degree of confluence are presented in Fig. 5. Unobscured observation of highly irregular individual particles shows that there exist three hierarchical levels of mineral particle aggregation: lateral, stacked and wedged, increasing in order of size. The smallest entity above the noise level that could be labeled is an acicular particle with a shorter dimension of 5 nm and a longer dimension of at least 30 nm. These acicular particles are consistent with the dimensions of the crystalline domains observed by TEM (Fig. 1A and D, filamentous motif). The extended needles show bending, with a curvature of approximately 100-150 nm, similar to the values observed for the crystals constituting the lacey pattern in Fig. 1E. The angular distribution of the needles is in the range of up to ± 20° relative to the main axis of the collagen fibrils in the original image (Fig. 2, filamentous portion in all panels), and thus they are similar to the azimuthal length of the (002) plane-related reflection arcs found in the diffraction patterns of the filamentous motif (Fig. 1A'). These filaments aggregate laterally, and form larger, platelet-shaped morphologies, and for that reason their maximal length cannot be reliably defined. The platelets often show longitudinal striations corresponding to the filament directions. Mostly, individual filaments are visible only at the fringes of a platelet (resembling the fingers of a hand), and in some cases, can be captured as self-standing entities. The platelet-shaped aggregates of acicular particles have two distinct features: they form stacks of two-to-four parallel platelets separated by a well-defined uniform gap of about 2 nm. Also, the platelet-shaped aggregates often show a gentle twist along their longitudinal axis, resembling the shape of a fan blade. Finally, platelets and their stacks converge into larger aggregates in such a way that the gap between them becomes wedge-shaped. These largest aggregates exceed the dimensions of the D-period and the interfibrillar spaces observed in 3D images of demineralized collagen in bone (*29*). Note that only the smallest converging aggregates are presented here, and these illustrate the lower limit of their dimensions – it must be kept in mind that most of the aggregates are more extended than those shown in Fig. 5 and Fig. S3. Apparently, these larger crystalline structures incorporating nested arrays of simpler acicular and platelet-shaped particles are not associated with only one collagen fibril, but rather they bridge between several of those, and can thus form an interlinked mineral network through cross-fibrillar mineralization.

Table 1: Description of hierarchically organized bone apatite crystals and their approximate sizes

Acicular crystal	Platelet	Stacks of platelets	Aggregates of stacks
Thin, subtly curved – 'fingers'	Irregular, flattened, formed of partly merging aligned acicular crystals – 'hand with fingers'	Two-to-four platelets separated by uniform gaps of 1-2 nm – 'pressed together hands'	Stacks of platelets and/or single platelets and/or individual acicular crystals coalescing at an angle
Base 5 nm, length 50-100nm	Thickness 5 nm, width 20-30 nm, length 50-100 nm	Thickness 20-40 nm, width 20-40 nm, length 100 nm	Complex irregular 3D shape, up to 200-300 nm

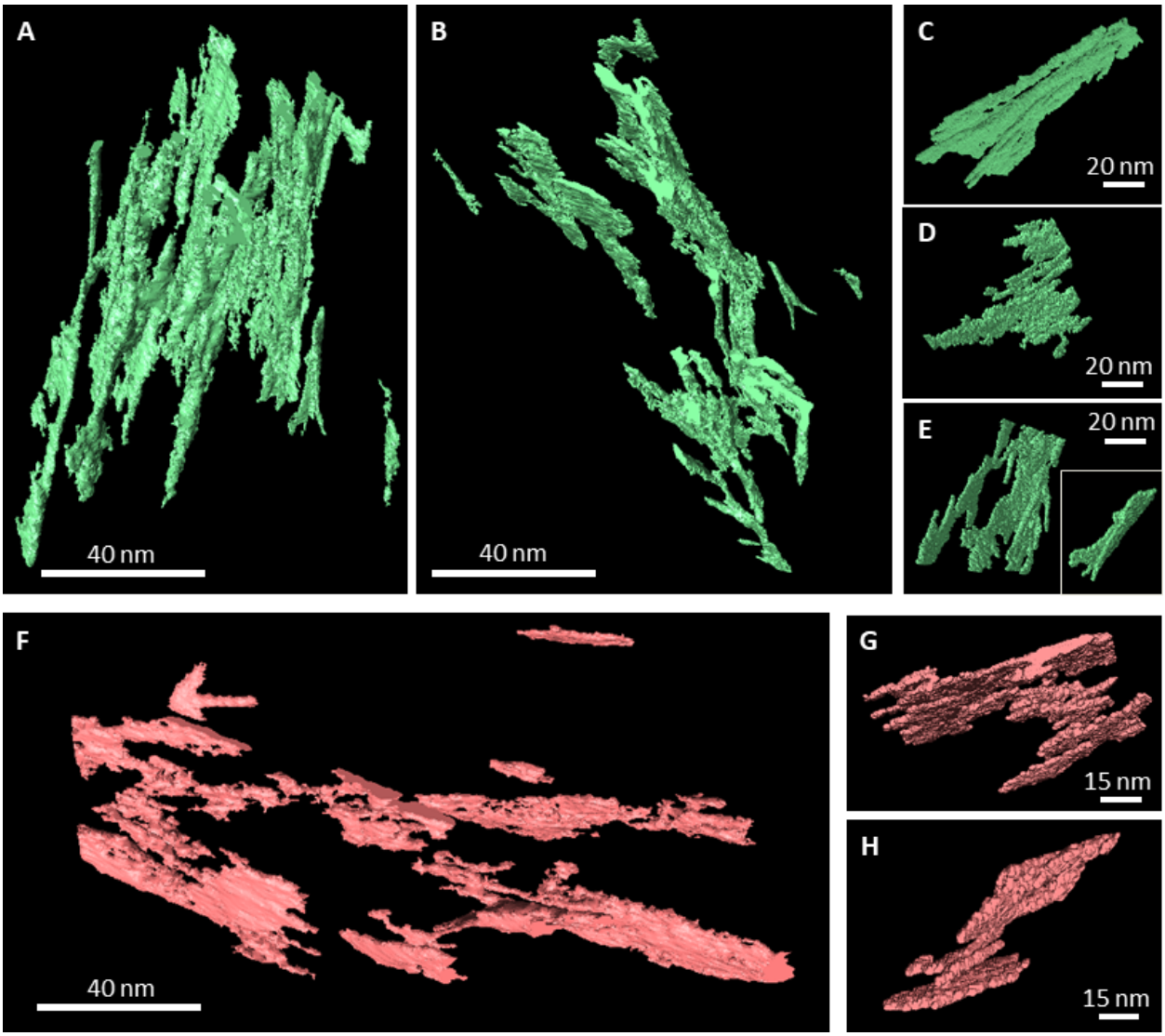

Figure 5: Evaluation of the tomogram shown in Fig. 2. Individual labels selected within the lacey pattern (A-E) and the filamentous pattern (F-H). Only the mineral aggregates that showed the least degree of confluence with each

other were selected. Panels (A) and (B) show the same ten labels in situ, in two different projections; panels (C – E) show four out of ten labels in individually adjusted projections to highlight their 3D shape. (F) Ten individual labels from the filamentous pattern, of which two are shown in adjusted projections, (G, H). There are 3 levels of confluence of mineral formations with each other: *i*) lateral merging of needle-shaped entities into platelets, *ii*) planar merging of platelet-shaped entities into stacks of 2-4 with a uniform gap between them, *iii*) merging of adjacent stacks at an angle (like fan blades, especially obvious in C, E, H) with a wedge-shaped clearance between them. Almost all labels in three dimensions show a delicate twist, especially visible in (B). The overall label density to the total-volume ratio was the same in both samples (approximately 0.45-0.5) – not to be confused with bone mineral density.

A three-dimensional model of mineral assembly

We applied the information obtained from both the 2D projections and the 3D electron tomography to construct a 3D model of the mineral phase as shown in supplemental video SV3. By relating the facts that *i*) there are three distinct projection patterns of crystalline assemblies, *ii*) the crystals are slightly curved, *iii*) the lacey pattern is already clearly visible when the filamentous projection is tilted by just 30-50° with respect to the fibrils' long axes, and *iv*) the collagen helices are staggered in a super-helical fashion (*5, 6, 39*), we suggest that apatite crystals within a continuous collagenous matrix follow an asymmetrical, subtly splaying pattern of organization, as illustrated in Fig. 6. The individual curved acicular mineral particles are partly aligned with the long axes of the collagen fibrils. Because of their curvature, and their longitudinal dimensions of 100 nm and more, these acicular mineral particles also splay away from the fibril, thus providing space for an adjacent tier of acicular particles along the collagen fibril axis. Thus, an intercalated cross-fibrillar network is formed, in which the acicular units are associated with the collagen fibrils and with the extrafibrillar space, and are likely associated with the neighboring collagen fibrils. Of note, the propensity of fine apatite crystals to splay away from a constraining fibril has been previously reported in vitro (*40*). For the sake of illustration clarity, the model of curved splaying acicular units does not reflect the fact that they partly coalesce laterally to form thin platelets, but their coalescence can be clearly observed in the tomographic images. Therefore, the model here underestimates the amount of extrafibrillar mineral. The subtle curvature of most acicular units, as noticeable in 2D and 3D images, is slightly accentuated in the model. The model viewed in the direction perpendicular to the collagen fibril axes (*i.e.*, fibrils in-plane) is congruent with the filamentous motif and provides a good explanation for the angular distribution of the crystals of approximately 20° relative to the fibril axis. The same model viewed in the direction almost aligned with the fibril axes (*i.e.* fibrils roughly out-of-plane) produces a lacey motif with lens-shaped holes surrounded by parallel

segments of curved filaments. Finally, the same model viewed exactly edge-on with respect to the collagen fibril axes results in concentric rosettes of cross-sections of the acicular units. To summarize, the same 3D structure – assembled arrays of curved, coarsely aligned acicular elements that splay away from one collagen fibril towards adjacent neighboring fibrils via the confined extrafibrillar space – explains the occurrence of all the motifs observed in 3D projections, as well as the 3D-rendered tomographic images.

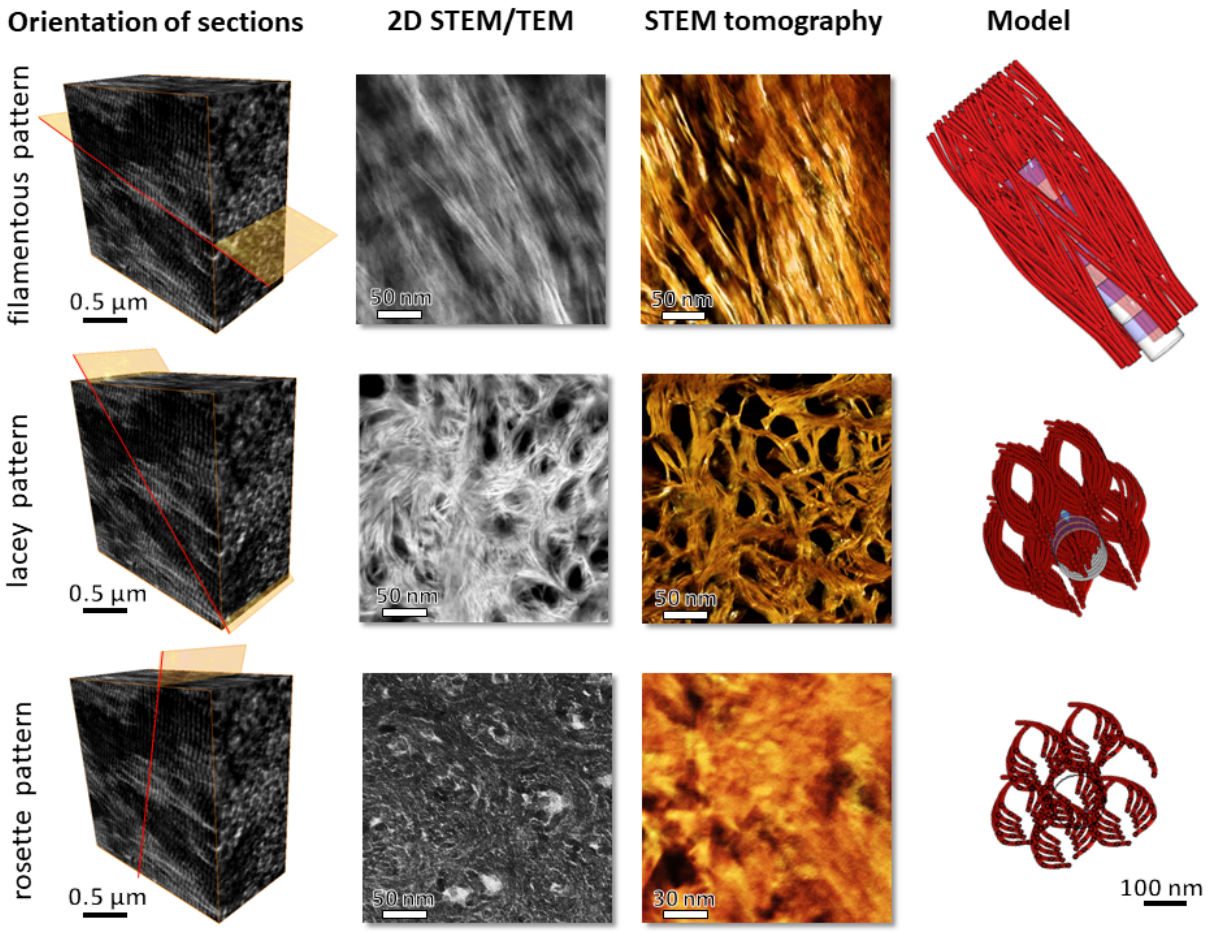

Figure 6: Proposed model of crystal organization in bone, and comparison with 2D projections obtained from TEM and STEM (second column of panels) and the tomogram reconstructed from the STEM tilt series (amber colored, third column of panels). The first column of panels shows the orientation of a thin specimen with respect to the ordered array of mineralized collagen fibrils in lamellar bone. The last column of panels features the same simplified 3D model of bone apatite crystals viewed in three different projections, in-plane, out-of-plane and edge-on views. For the sake of clarity, note that the model drawing has fewer concentric tiers of curved filaments than it presumably would accommodate.

The repercussions of this hierarchical mineral/collagen assembly pattern are manifold, affecting the mechanical properties of bone as well as the metabolic role of the carbonated apatite phase as a reservoir for mobilization and sequestration of inorganic ions (*41*). The uniform gaps between the platelet-shaped formations are known to contain disordered calcium phosphate, structural water (*42, 43*) and possibly noncollagenous proteins (*44*) and polysaccharides (*19*). These unstructured sheaths maintain the uniform high aspect ratio of individual crystallites, which contribute to their flexibility and toughness, and their reduced sensitivity to stress-induced crack formation – a feature characteristic for the mechanical behavior of high aspect ratio structures, for example, of nanotubes or nano-whiskers (*45*). From the mechanical perspective of composite materials theory, a high aspect ratio of staggered filler units within the matrix, together with a high density of the filler units, both contribute to higher material strength and stiffness (*46*). Notably, in bone the high aspect ratio of the thin elongated crystals is purposefully maintained by the rigid layers of structural water between neighboring mineral particles (*42, 43, 47*), whereas the loss of structural water from bone tissue is associated with age-related decay of bone mechanical properties (*48*).

The mechanism by which acicular crystals merge to form platelets remains unclear. In concert with the theory of biomineralization occurring through an amorphous precursor stage (*49, 50*), , the crystallization of biological apatite could be expected to proceed along the path of least interference within a crosslinked collagenous matrix that is rich in mineralization inhibitors that regulate crystal growth. The formation of an ordered crystalline phase throughout the amorphous template can be locally disrupted by the presence of noncollagenous organic entities (*51*), significant amounts of bound water and inorganic impurities (*14, 17*), as well as by pre-stress of the collagenous matrix (*52*). It is still an unknown as to whether acicular crystals merge into platelets or whether thin pre-stressed platelets split into acicular crystals at their periphery. The interfacial role of water is mediated by numerous organic inclusions (*9, 19*) and inorganic impurities (*14*), both of which can disrupt the long-range order of bone apatite.

The higher-level coalescence of stacks of platelets into larger wedged aggregates is an illustration of continuity of the mineral phase transversely spanning the dimensions of more than one collagen fibril. The collagenous matrix of bone is extensively crosslinked by intermolecular covalent bonds (*53*). In bone, as opposed to tendon for example, it is difficult to discern individual collagen fibrils and their trajectories because they are all aligned in register. To examine the true length of individual collagen fibril segments, we performed manual labeling of FIB-SEM-imaged demineralized bone collagen fibrils in a digitally resliced edge-on orientation. Figure 7 and supplemental video SV4 show that individual fibrils can only be tracked along a segment length of on average 200 nm before they split or merge with other fibrils, thus effectively forming a continuous 3D network. Since individual fibrils are integrated into a continuous network, both fibril segments and extrafibrillar spaces are of a finite length, rarely exceeding a few hundreds of nanometers. It could be coincidental that the average segment length of the collagen network, and the maximal size of a mineral aggregate, are in fact of

similar values. However, it is possible that the longitudinal dimension of the extrafibrillar space serves as a limiting factor influencing the extent of mineral aggregation. Such a physical confinement is in accord with the need to keep mineral particles small in order to optimize material toughness. This observation is also consistent with the significant crystallite growth in bone observed in the process of diagenesis and postmortem decay of organic matter (*54*).

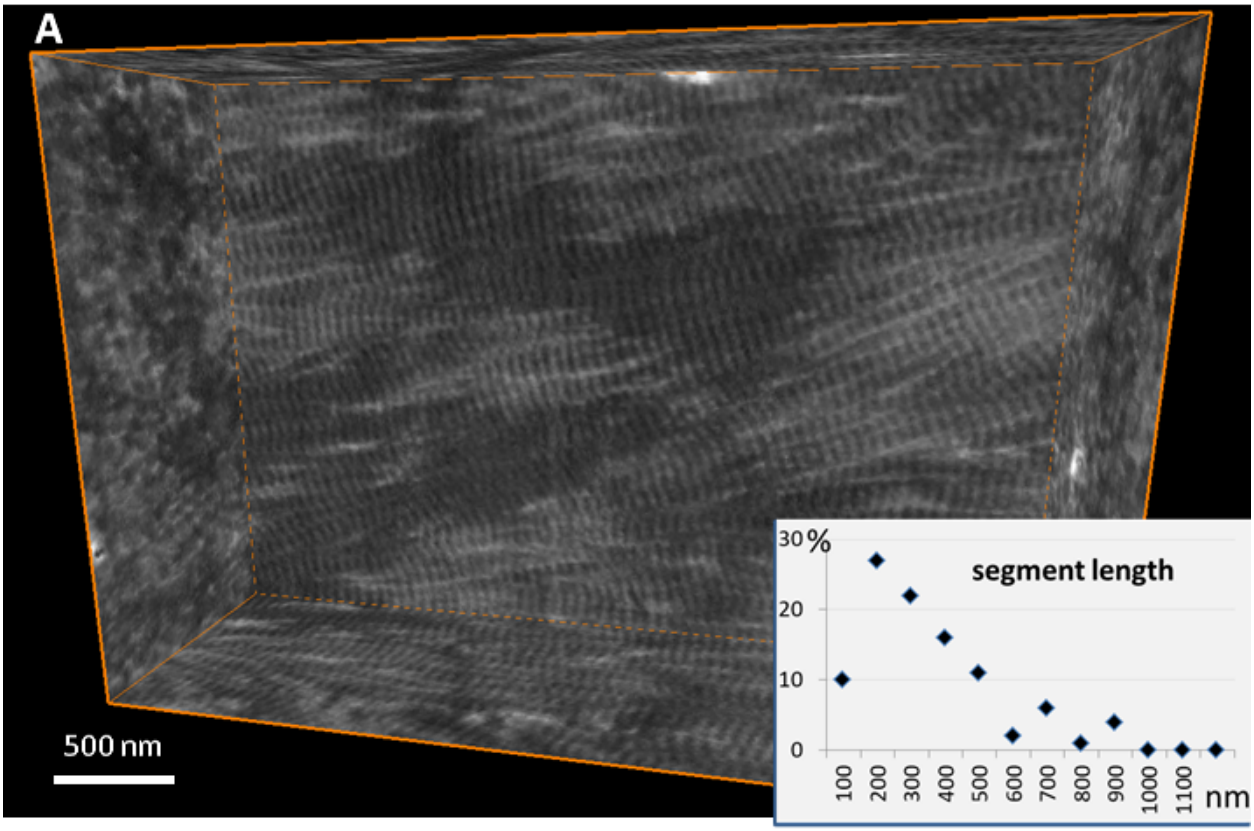
A
500 nm
30 %
segment length
20
10
0
100
200
300
400
500
600
700
800
900
1000
1100
nm

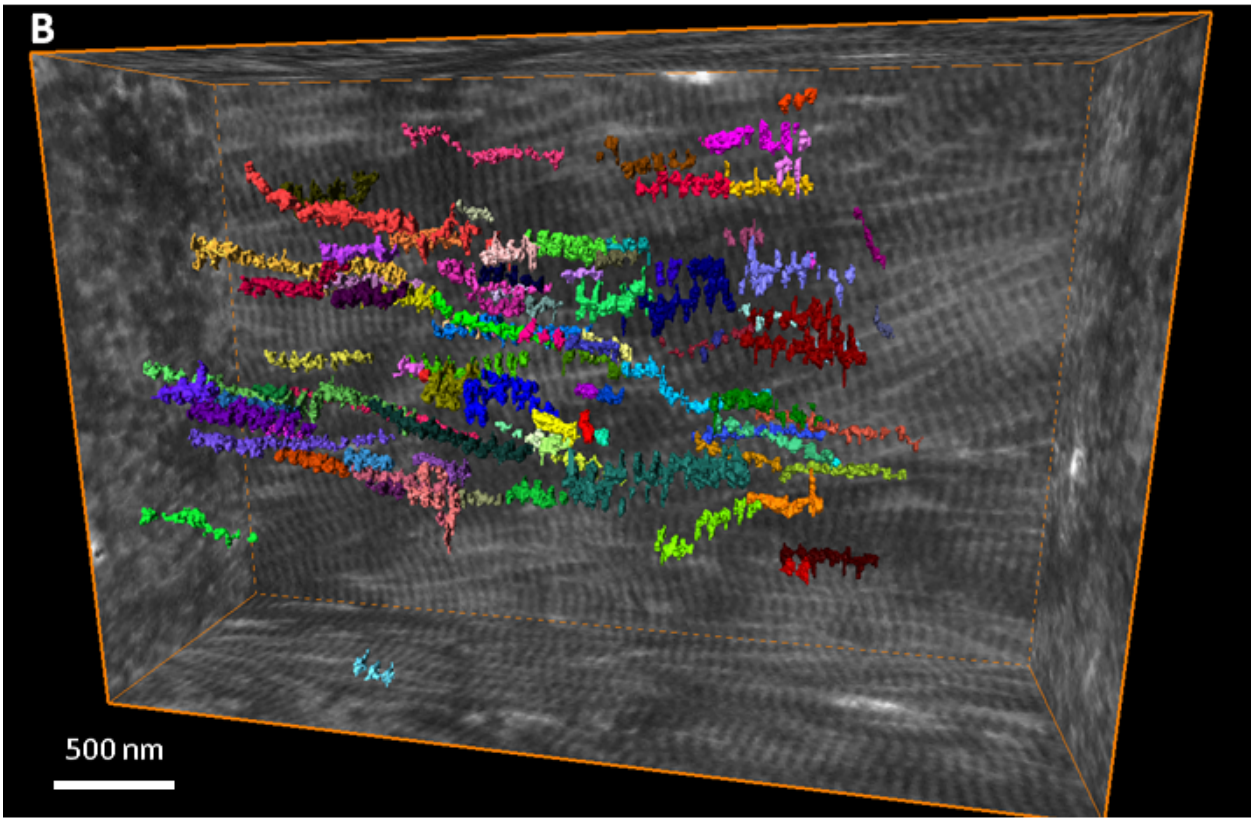
B
500 nm

Figure 7: Discernible segment length of collagen fibrils in the extracellular matrix of bone. (A) Reconstructed volume of demineralized and stained collagen fibrils in bone, and (B) individual fibrils color-labeled where they can be continuously traced in the edge-on view. Each of 100 labels is shown in a different color visualizing the distribution of segment lengths.

Although the mechanisms of collagen crosslinking into a continuous framework, and the mechanisms of crystallite aggregation, are obviously different, the final results converge to provide for the continuity of bone tissue's organic and inorganic components. The preservation of bone morphology at multiple scales has been previously demonstrated using specimens treated by deproteinization or demineralization in hydrated conditions (*55, 56*).

The impact of morphology on the effective mineral surface area

The small size of bone crystallites has been reported to contribute to the substantial surface area of mineral in the human skeleton which is in the order of 0.1 km^2/kg (*57-59*), based on gas absorption experiments. Interestingly, the effective mineral surface area reportedly decreases at a temperature exceeding 300°C when the loss of bound water and charring of organic constituents occur, indicating crystal merging (*59*). To quantitatively compare the impact of the mineral morphology on the total surface area we calculated the total crystallite specific surface area from

$$a_{i,tot} = 0.32 \frac{A_i}{\rho_{AP} V_i}$$

where A_i and V_i are the area and volume of the respective crystal morphology and ρ_{AP} is the density of the apatite phase. For platelet shaped crystals we find

$$a_{PL} = \frac{0.64}{\rho_{AP}} \left(\frac{1}{w} + \frac{1}{d} + \frac{1}{t} \right)$$

with average crystallite dimensions w, d and t, whereas for the acicular morphology the surface per mass unit can be calculated from

$$a_{AC} \approx \frac{1.48}{\rho_{AP} d}$$

with d being in this case the acicular crystallite cross-sectional diameter.

Using an apatite density of 3,190 kg/m^3 and a typical mineral content of the skeleton amounting to 32 wt% (*60*) (not to be confused with 67 wt% in mineralized extracellular matrix of bone (*61*)

usually assumed for a dissected, defatted and dry specimen) these values were used to calculate the specific surface area for a thin platelet of 5 × 25 × 100 nm to be compared with the value obtained for acicular crystallites of 5 nm cross-sectional diameter and 100 nm length. We find that for an average-size human (having a total skeleton mass of roughly 10 kg, of which about 32% is ash (*60*)), the total surface area of the acicular bone crystallites is approx. 0.9 km^2 (for comparison, this is about twice the area of Vatican City, and is consistent with the estimates in (*57, 59*) based on gas adsorption measurements). In contrast, if the bone mineral geometry would be plate-shaped, with the crystal size being 5 × 20 × 100 nm, the total surface area would be almost 40% lower, which is incongruent with the gas adsorption experiments. In order to validate the surface area dependence on imaging resolution, we calculated the surface-to-volume ratio of the 3D-rendered mineral as a function of pixel size. The original pixel size in the3D tomographic images was 0.98 nm and it was digitally coarsened to 5 nm, a decrease of resolution where the acicular elements could not be clearly visualized, but the plate-shaped aggregates could still be well defined. Interestingly, in the tomogram with the pixel size artificially coarsened from less than 1 nm to 5-6 nm, the surface-to-volume ratio was 40% lower compared to the original resolution (*i.e.*, at which the acicular crystals were well resolved, see Fig. S4).

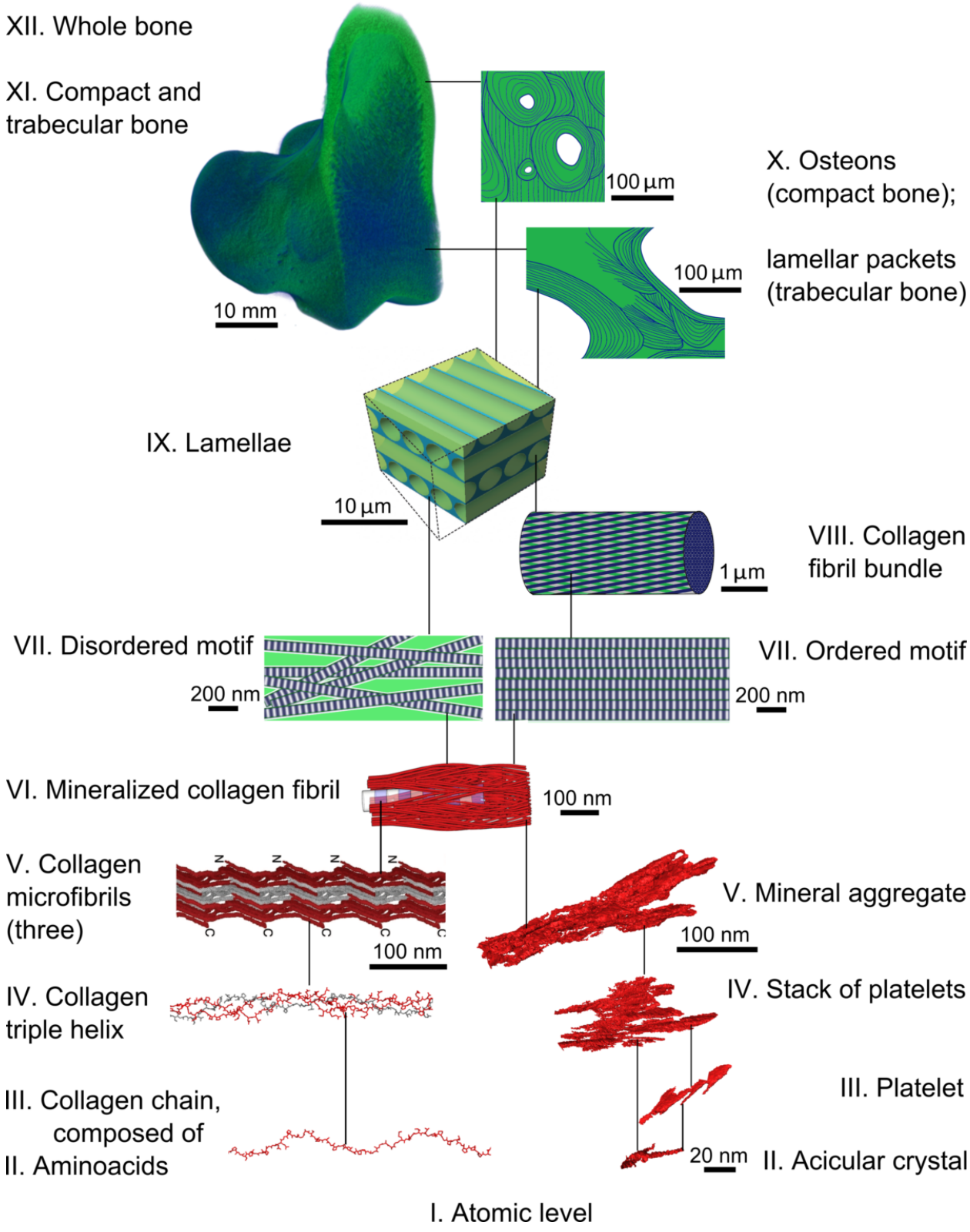
XII. Whole bone
XI. Compact and trabecular bone
10 mm
100 µm
X. Osteons (compact bone);
100 µm
lamellar packets (trabecular bone)
IX. Lamellae
10 µm
1 µm
VIII. Collagen fibril bundle
VII. Disordered motif
200 nm
VII. Ordered motif
200 nm
VI. Mineralized collagen fibril
100 nm
V. Collagen microfibrils (three)
100 nm
V. Mineral aggregate
100 nm
IV. Collagen triple helix
IV. Stack of platelets
III. Collagen chain, composed of
II. Aminoacids
III. Platelet
20 nm
II. Acicular crystal
I. Atomic level

Figure 8: A new scheme of hierarchical organization in bone. For levels VII-XII (green) see Reznikov et al. (*4, 29, 62*). Both ordered and disordered motifs of lamellar bone comprise mineralized collagen fibrils (VI) that are 80-120 nm thick and form a continuous network. Collagen fibrils are composed of quasi-hexagonally packed microfibrils (V), each of which incorporates multiple staggered triple helices (IV) that in turn are formed from repetitive chains (III) of amino acids (II). Collagen levels V to II are discussed in detail by Orgel et al. (*5, 35, 39, 63, 64*). Collagen panels III and IV are courtesy of Dr. Joseph Orgel. The inorganic component of the mineralized collagen fibrils (VI) itself incorporates several nested structural motifs, listed as follows in decreasing order of complexity: mineral aggregates (V), stacks of platelets (IV), platelets (III) and acicular crystals (II).

Fractal-like hierarchical bone architecture

The hierarchical assembly of the organic and inorganic components of bone is implemented in a bottom-up manner through the interactions between cells and the extracellular matrix, during growth, development and maintenance. However, the paradigm of bone hierarchy was first elaborated using a top-down approach by the English physician Clopton Havers who in 1691 first distinguished five nested structural levels spanning from a bone's anatomy to its basic components: the "earth" (organic matter) and the "fixed salt" (inorganic matter) (*65*). Major methodological leaps have enriched our concept of bone hierarchy – the key review by Weiner and Wagner in 1998 described seven nested levels of organization (*66*). With the advent of nanoscale 3D imaging, nine hierarchical levels were defined in 2014 (*4*). Based on the present work, three more levels can be added to the existing scheme as shown in Fig. 8. The demonstration of bone mineral as a hierarchical phase on its own, consisting of acicular, plate-shaped, stacked and aggregated assemblies, helps to clarify the mechanism of bone toughness and structural integrity (although it does not completely explain how the nested assemblies of crystals become intercalated with the organic phase). A comparison with previous works illustrates that the helical motif repeats itself on every scale of bone architecture, and pertains to both collagen and mineral. That crystals may curve and bend may appear counterintuitive, it is nevertheless possible in light of the crystals' high aspect ratio, their formation via an amorphous precursor stage, and their location within a pre-stressed hydrated matrix. Also, the shallow-pitch helical morphology puts bone mineral crystals in line with the nested self-affine helical motifs found throughout the hierarchy of bone structure in general.

As Nature uses and re-uses effective strategies (*67*), and as helical motifs are abundant in shells, horns, cones and spider webs (*8*) amongst other biological structures, we suggest that the fractal-like organization (*i.e.*, the self-affine helical motif occurring across multiple scales) is another way to further optimize bone mechanical attributes over millions of years of evolutionary refinement.

Methods

Samples and preparation

Our study focused on compact lamellar bone samples prepared from the proximal femur of two female individuals, 48 and 50 years old. The Imperial College Tissue Bank (application R13004) approved collection and research of excess human tissue from surgeries performed at Charing Cross Hospital (London, UK). The proximal femur samples were collected from elective arthroplasty patients when written informed consent was obtained. The lower femoral necks, also referred to as the "calcar" area, were cut in two planes, along and across the long axis, so that compact bone osteons would be cut in both long- and cross-sections. The resulting sample sections were polished, and shallow ridges of osteonal lamellae were identified by optical microscopy. The polished bone samples were defatted in acetone and embedded in Epon (Electron Microscopy Sciences, USA) in vacuum – embedding in vacuum was conducted in order to fill bone porosities with a solid medium. The top surface of the embedded samples was exposed with a glass knife and a diamond knife in order to visualize osteonal lamellae as shallow ridges oriented in concentric circles (transverse osteon section) or as a parallel series (longitudinal osteon section).

Ion-beam milling in an FIB-SEM provides precise ablation of the mineralized substrate and controlled thinning of the area of interest until electron transparency is obtained. We prepared 100 nm-thick specimens by FIB milling and the lift-out technique, using a Helios Nanolab 600, FEI, USA, following an automated procedure (AutoTEM G2 software, FEI, The Netherlands) at 30 keV. The real-time visual control of the milling and thinning processes in the FIB-SEM allows for the preparation of a TEM specimen in the desired orientation (perpendicular to the lamellar planes for both configurations) and sufficiently distanced from the osteocyte lacunae. Specimens were mounted on a semi-grid for thinning to obtain electron transparency (approximating a 100 nm section thickness) using current reduction from 0.46 nA to 28 pA, at 30 keV. Final polishing of the thinned samples was conducted at ion acceleration voltages of 16 keV and then 5 keV, using at the same time electron currents sufficient for visual control in order to gently remove surface unevenness, redeposited debris and the products of local mineral amorphization. Using an appropriate sequence of decreasing voltage and current values prevents ion beam-related artifacts (*68*) and allows for the best possible preservation of the structural features of the sample, which is especially important for specimens containing organic-inorganic interfaces (*32*) and components sensitive to contact with water (*22*).
The TEM investigation of the ultrastructure of bone followed a two-pronged approach using bright-field and high-resolution TEM in conjunction with selected-area electron diffraction (SAED) to obtain and characterize 2D projections of the crystal structure. STEM tomography was used to identify the 3D assembly pattern particularly of the mineral phase in unmodified air-dried bone embedded in epoxy resin in vacuum.

Transmission electron microscopy

For 2D imaging of cross-sections, we used a conventional JEOL 2011 TEM as well as a JEOL 2200 FS TEM operating in the STEM mode with a 3rd-order probe aberration corrector and a high-angle annular dark field imaging detector (inner collection angle 110 mrad). Both microscopes were operated at a 200 kV acceleration voltage. For diffraction pattern collection and high-resolution imaging, we notably found the use of an LaB_6 electron source beneficial compared to a field emission gun source since this, due to the lower spatial electron coherence, minimizes damage by the electron beam.

The appropriate choice of imaging conditions for observing the details of the mineral/organic organization in bone constitutes a major challenge. For TEM analyses, low electron doses are required to avoid material ablation and re-deposition during imaging (*69*). Generally, STEM allows for better contrast at low beam exposure compared to plane-view TEM, and is thus less prone to producing artifacts of this type (*69*). In addition, STEM provides directly interpretable contrast, and is therefore also preferable for tomography since plane-view TEM imaging depends strongly on Bragg contrast. Since the local contrast depends on the sample orientation tomographic imaging is difficult and the achievable spatial resolution is limited. For this reason, STEM methodology is preferable over the TEM methodology for 3D tomographic imaging of polycrystalline samples, such as bone.

STEM Tomography

We used scanning transmission electron microscopy (STEM), an imaging approach sensitive to variations in the atomic number *Z*, thus enabling the simultaneous imaging of collagen and mineral phases in situ. Furthermore, tomographic sample tilting in the STEM mode allows 3D imaging with nanometer-level resolution (*70*) as required for the small dimensions of the apatite crystals.

Tomography was performed using an FEI Tecnai Osiris STEM (X-FEG Schottky field emitter) operated at 200 kV, 245 µA, using a Fischione 2020 advanced tomography holder with a previous data set obtained using manual tilt at a JEOL 2200 FS (*71*). The image size acquired at 0.5 nA was 2048 × 2048 pixels, with a total acquisition time of 2.15 s per frame as follows: area search (0.15 s), focus (0.5 s), exposure (1 s) and tracking (0.5 s), automated and equal for each frame. Data were acquired using the FEI Tecnai Osiris using the FEI Xplore3D and Inspect3D acquisition, post-alignment and reconstruction software. To produce the resulting 3D volumes, the tilt series was then processed using the IMOD software package (http://bio3d.colorado.edu/imod/) using the filtered back-projection algorithm without applying fiducial markers. We subsequently used the FEI Avizo 9.2 software for 3D rendering and segmentation.

FIB-SEM tomography

The FIB-SEM tomography workflow is described in (*29*). Briefly, the bone sample was demineralized in parallel with mild fixation (*72*), conditioned with alcian blue to stabilize noncollagenous organic components, fixed with glutaraldehyde, and stained with osmium tetroxide (OTOTO protocol). The sample was high-pressure frozen and freeze-substituted, which preserves the dimensions and architecture as in the hydrated state. The sample was then embedded in Epon and sectioned, and imaging was performed using a dual-beam FEI Helios 600 Nanolab FIB-SEM operating in the serial-surface view mode with the slice thickness equal to the lateral resolution of the 2D images in the stack, being approximately 10 nm at 30 keV, 86 pA. The stack was aligned using Fiji (NIH, USA) (*73*). Labeling of individual collagen fibrils was carried out using the local threshold algorithm in Avizo 9.2, FEI, USA. For the current study, the stack of adult human osteonal lamellar bone (originally referred as M77) was used for collagen segment tracing. An area of well-aligned, ordered, nearly horizontal collagen fibrils within one lamella was selected. In the edge-on projection, a cross-section of a fibril was labeled based on the local gradient and then traced in both directions until the same cross-section could not be identified. In this manner, one hundred of collagen fibril segments were traced, their length was recorded in nanometers and the distribution histogram of the segment length values was analyzed.

Specific surface area and crystallite morphologies

Mineral morphology in bone has important implications because of the resulting high surface area and its adsorption capacity, particularly for water molecules. The surface area, volume and mass of a single-crystal platelet having dimensions w, d and t is

$$A_{PL} = 2 \cdot \left(w \cdot d + w \cdot t + d \cdot t \right)$$

The volume of an individual platelet is

$$V_{PL} = w \cdot d \cdot t$$

And the platelet mass is

$$M_{PL} = \rho_{AP} V_{PL}$$

with ρ_{AP} being the mass density of the bone apatite.

For an acicular crystal with hexagonal symmetry where the crystal length l is much larger than its lateral extension d, we find

$$A_{AC} = 3 \cdot d \cdot l + \sqrt{27} \cdot \left(\frac{d}{2} \right)^2 \approx 3 \cdot d \cdot l$$

The volume of an individual (acicular) needle is

$$V_{AC} = \frac{\sqrt{27}}{2} \cdot \left(\frac{d}{2}\right)^2 \cdot l$$

And the needle mass is

$$M_{AC} = \rho_{AP} V_{AC}$$

To obtain the total surface area resulting from the specific geometries it is necessary to multiply the surface area of the individual crystals by 0.32 (32 wt% mineral content) and the number of crystals constituting the mineral phase (which is the ratio of the total mineral mass divided by the mass of an individual crystal). Thus,

$$A_{i,tot} = 0.32 \frac{M_{tot}}{\rho_{AP}} \frac{A_i}{V_i}$$

with the index representing either a plate-shaped or acicular geometry. This results in the following expressions for the total specific surface areas for both geometries:

$$A_{PL,tot} = 0.64 \frac{M_{tot}}{\rho_{AP}} \left(\frac{1}{w} + \frac{1}{d} + \frac{1}{t}\right)$$

$$A_{AC,tot} = 0.32 \frac{M_{tot}}{\rho_{AP}} \frac{24}{\sqrt{27} \cdot d}$$

The respective specific areas per mass a_{PL} and a_{AC} are given by the total areas divided by the total masses.

References

1. T. A. Cook, *The Curves of Life Being an Account of Spiral Formations and Their Application to Growth in Nature, to Science and to Art, With Special Reference to the Manuscripts of Leonardo Da Vinci*. (Constable and Company Ltd., London, 1914).
2. J. Hert, P. Fiala, M. Petrtyl, Osteon orientation of the diaphysis of the long bones in man. *Bone* **15**, 269 (1994).
3. W. Wagermaier *et al.*, Spiral twisting of fiber orientation inside bone lamellae. *Biointerphases* **1**, 1 (2006).
4. N. Reznikov, R. Shahar, S. Weiner, Bone hierarchical structure in three dimensions. *Acta Biomaterialia* **10**, 3815 (2014).
5. J. P. R. O. Orgel, T. C. Irving, A. Miller, T. J. Wess, Microfibrillar structure of type I collagen in situ. *PNAS* **103**, 9001 (2006).
6. J. P. R. O. Orgel *et al.*, The in situ supermolecular structure of type I collagen. *Structure* **9**, 1061 (2001).
7. B. Mandelbrot, How long is the coast of Britain? Statistical self-similarity and fractional dimenstion. *Science* **156**, 636 (1967).

8. D. W. Thompson, *On Growth and Form*. (Cambridge University Press, Cambridge, ed. 2nd, 1942), pp. 1116.
9. A. George, A. Veis, Phosphorylated proteins and control over apatite nucleation, crystal growth, and inhibition. *Chem Rev* **108**, 4670 (2008).
10. F. Betts, N. C. Blumenthal, A. S. Posner, Bone mineralization. *Journal of Crystal Growth* **53**, 63 (1981).
11. J. C. Elliott, Hydroxyapatites and nonstoichiometric apatites. *Studies in Inorganic Chemistry* **18**, 111 (1994).
12. E. Bonnucci, in *Advanced Topics on Crystal Growth*. (2013).
13. J. Mahamid *et al.*, Bone mineralization proceeds through intracellular calcium phosphate loaded vesicles: a cryo-electron microscopy study. *J Struct Biol* **174**, 527 (2011).
14. E. Davies *et al.*, Citrate bridges between mineral platelets in bone. *PNAS*, E1354 (2014).
15. K. Chatzipanagis *et al.*, Crystallization of citrate-stabilized amorphous calcium phosphate to nanocrystalline apatite: a surface-mediated transformation. *Cryst Eng Comm*, (2016).
16. D. E. Rodriguez *et al.*, Multifunctional role of osteopontin in directing intrafibrillar mineralization of collagen and activation of osteoclasts. *Acta Biomaterialia* **10**, (2014).
17. Y.-Y. Hu, A. Rawal, K. Schmidt-Rohr, Strongly bound citrate stabilizes the apatite nanocrystals in bone. *PNAS* **107**, 22425 (2010).
18. J. D. Termine, A. S. Posner, Amorphous/crystalline interrelationships in bone mineral. *Calcif. Tiss. Res.* **1**, 8 (1967).
19. E. R. Wise *et al.*, The organic-mineral interface in bone is predominantly polysaccharide. *Chem Mater* **19**, 5055 (2007).
20. C. Jaeger *et al.*, Investigation of the nature of the protein-mineral interface in bone by solid-state NMR. *Chem Mater* **17**, 359 (2005).
21. B. Wopenka, J. D. Pasteris, A mineralogical perspective on the apatite in bone. *Materials Science and Engineering C* **25**, 131 (2005).
22. C. Rey, C. Combes, C. Drouet, M. J. Glimcher, Bone mineral: update on chemical composition and structure. *Osteoporosis Int* **20**, 1013 (2009).
23. H. Fernandez-Moran, A. Engstroem, Electron microscopy and X-ray diffraction of bone. *Biochim Biophys Acta* **23**, 260 (1957).
24. A. L. Arsenault, M. D. Grynpas, Crystals in calcified epiphyseal cartilage and cortical bone of the rat. *Calcif Tissue Int* **43**, 219 (1988).
25. W. Traub, T. Arad, S. Weiner, Origin of mineral crystal growth in collagen fibrils. *Matrix* **12**, 251 (1992).
26. M. J. Glimcher, Molecular biology of mineralized tissues with particular reference to bone. *Rev. Mod. Phys.* **31**, 359 (1959).
27. S. Weiner, W. Traub, H. D. Wagner, Lamellar bone:structure-function relations. *J. Struct. Biol.* **126**, 241 (1999).
28. E. A. McNally, H. P. Schwarcz, G. A. Botton, A. L. Arsenault, A model for the ultrastructure of bone based on electron microscopy of ion-milled sections. *PLoS ONE* **7**, (2012).
29. N. Reznikov, R. Shahar, S. Weiner, Three-dimensional structure of human lamellar bone: the presence of two different materials and new insights into the hierarchical organization. *Bone* **59**, 93 (2014).
30. E. McNally, F. Nan, G. A. Botton, H. P. Schwartcz, Scanning transmission electron microscopic tomography of cortical bone using Z-contrast imaging. *Micron*, (2013).
31. B. A. Cressey, G. Cressey, A model for the composite nanostructure of bone suggested by high-resolution transmission electron microscopy. *Mineralogical Magazine* **67**, 1171 (2003).
32. V. Jantou, M. Turmaine, G. D. West, M. A. Horton, D. W. McComb, Focused ion beam milling and ultramicrotomy of mineralised ivory dentine for analytical transmission electron microscopy. *Micron* **40**, 495 (2009).
33. D. S. Bocciarelli, Morphology of crystallites in bone. *Calc Tiss Res* **5**, 261 (1970).

34. H. P. Schwarcz, The ultrastructure of bone as revealed in electron microscopy of ion-milled sections. *Seminars in Cell Developmental biology* **46**, 44 (2015).
35. J. P. R. O. Orgel, J. D. San Antonio, O. Antipova, Molecular and structural mapping of collagen fibril interactions. *Connect Tissue Res* **52**, 2 (2011).
36. J. R. Kremer, D. N. Mastronarde, J. R. McIntosh, Computer visualization of three-dimensional image data using IMOD. *J Struct Biol* **116**, 71 (1996).
37. N. Reznikov, R. Almany-Magal, R. Shahar, S. Weiner, Three-dimensional imaging of collagen fibril organization in rat circumferential lamellar bone using a dual beam electron microscope reveals ordered and disordered sub-lamellar structures. *Bone* **52**, 676 (2013).
38. J. Serra, *Image Analysis and Mathematical Morphology*. (Academic Press Inc., Orlando, FL, USA, 1983).
39. J. P. R. O. Orgel, A. V. Persikov, O. Antipova, Variation in the Helical Structure of Native Collagen. *PLoS ONE* **9**, (2014).
40. M. J. Olszta *et al.*, Bone structure and formation: a new perspective. *Mat. Sci. Engn. R* **58**, 77 (2007).
41. N. Reznikov, J. A. M. Steele, P. Fratzl, M. M. Stevens, A materials science vision of extracellular matrix mineralization. *Nature Reviews Materials*, (2016).
42. M. J. Duer, The contribution of solid-state NMR spectroscopy to understanding biomineralization: Atomic and molecular structure of bone. *J Magn Reson* **253**, 98 (2015).
43. Y. Wang *et al.*, Water-mediated structuring of bone apatite. *Nature Materials* **12**, 1144 (2013).
44. M. D. McKee, M. T. Kaartinen, in *Aging, Osteoporosis and Dental Implants,* G. Zarb, Lekholm, U., Albrektsson, T., Tenenbaum, H., Ed. (Quintessence Pub. Co., Carol Stream, IL, USA, 2002).
45. S. Iijima, C. Brabec, A. Maiti, J. Bernholc, Structural flexibility of carbon nanotubes. *J Chem Phys* **104**, 2089 (1996).
46. B. Bar-On, H. D. Wagner, New insights into the Young's modulus of staggered biological composites. *Materials Science and Engineering C* **33**, 603 (2013).
47. M. A. Fernandez-Seara, S. L. Wehrli, F. W. Wehrli, Diffusion of exchangeable water in cortical bone studied by nuclear magnetic resonance. *Biophysical Journal* **82**, 522 (2002).
48. J. S. Nyman, Q. Ni, D. P. Nicolella, X. Wang, Measurements of mobile and bound water by nuclear magnetic resonance correlate with mechanical properties of bone. *Bone* **42**, 193 (2008).
49. L. B. Gower, Biomimetic model systems for investigating the amorphous precursor pathway and its role in biomineralization. *Chem Rev* **108**, 4551 (2008).
50. J. Mahamid *et al.*, Mapping amorphous calcium phosphate transformation into crystalline mineral from the cell to the bone in zebrafish fin rays. *PNAS* **107**, 6316 (2010).
51. M. D. McKee, M. Murshed, M. T. Kaartinen, in *Mineralized Tissues in Oral and Craniofacial Science: Biological Principles and Clinical Correlates,* L. K. McCauley, Somerman. M.J., Ed. (John Wiley & Sons, 2012).
52. L. Bertinetti *et al.*, Osmotically driven tensile stress in collagen-based mineralized tissues. *J Mech Behav Biomed Mater* **52**, 14 (2015).
53. D. R. Eyre, Dickson, I.R., Van Ness, K., Collagen cross-linking in human bone and articular cartilage. *Biochem J* **252**, 495 (1988).
54. T. J. Wess *et al.*, Microfocus small angle X-ray scattering reveals structural features in archaeological bone samples: Detection of changes in bone mineral habit and size. *Calcif Tissue Int* **70**, 103 (2001).
55. V. Benezra Rosen, L. W. Hobbs, M. Spector, The ultrastructure of anorganic bovine bone and selected synthetic hyroxyapatites used as bone graft substitute materials. *Biomaterials* **23**, 921 (2002).
56. P.-Y. Chen, D. Toroian, P. A. Price, J. McKittrick, Minerals form a continuum phase in mature cancellous bone. *Calcif Tissue Int* **88**, 351 (2011).
57. J. M. Holmes, R. A. Beebe, Surface areas by gas adsorption on amorphous calcium phosphate and crystalline hydroxyapatite. *Calc Tiss Res* **7**, 163 (1971).

58. J. C. Elliott, Calcium phosphate biominerals. *Rev. Geochem. Mineral.* **48**, 427 (2002).
59. A. S. Posner, R. A. Beebe, The surface chemistry of bone mineral and related calcium phosphates. *Seminars in Arthritis and Rheumatism* **4**, 267 (1975).
60. H. H. Mitchell, T. S. Hamilton, F. R. Steggerda, H. W. Bean, The chemical composition of the adult human body and its bearing on the biochemistry of growth. *J Biol Chem* **158**, 623 (1945).
61. J. D. Currey, *Bones: Structure and Mechanics* (Princeton University Press, Oxford, ed. 2nd ed., 2002).
62. N. Reznikov, H. Chase, V. Brumfeld, R. Shahar, S. Weiner, The 3D Structure of the collagen fibril network in human trabecular bone: relation to trabecular organization. *Bone* **71**, 189 (2015).
63. J. P. R. O. Orgel, T. J. Wess, A. Miller, The in situ conformation and axial location of the intermolecular cross-linked non-helical telopeptides of type I collagen. *Structure* **8**, 137 (2000).
64. J. P. R. O. Orgel, A. Eid, O. Antipova, J. Bella, J. E. Scott, Decorin core protein (Decoron) shape complements collagen fibril surface structure and mediates its binding. *PLoS ONE* **4**, (2009).
65. C. Havers, *Osteologia Nova*. (Samuel Smith, London, 1691).
66. S. Weiner, H. D. Wagner, The material bone: structure- mechanical function relations. *Ann. Rev. Mat. Sci.* **28**, 271 (1998).
67. P. Pearce, *Structure in Nature Is a Strategy for Design*. (MIT Press, Boston, MA, USA, 1990).
68. J. Mayer, L. A. Giannuzzi, T. Kamino, J. Michael, TEM sample preparation and FIB-induced damage. *MRS Bulletin* **32**, 400 (2007).
69. D. B. Carlson, J. E. Evans, in *The Transmission Electron Microscope,* K. Maaz, Ed. (InTech, 2012), pp. 85-97.
70. P. A. Midgley, M. Weyland, 3D electron microscopy in the physical sciences: the development of Z-contrast and EFTEM tomography. *Ultramicroscopy* **96**, 413 (2003).
71. L. Lari, I. Wright, E. D. Boyes, DIY Tomography sample holder. *Journal of Physics: Conference Series* **644**, (2015).
72. M. D. McKee *et al.*, Effects of fixation and demineralization on the retention of bone phosphoprotein and other matrix components as evaluated by biochemical analyses and quantitative immunocytochemistry. *J Bone Miner Res* **6**, 937 (1991).
73. J. Schindelin *et al.*, Fiji: an open-source platform for biological-image analysis. *Nature Methods* **9**, 676 (2012).

Acknowledgements

This work was carried out in the framework of the projects SMILEY (FP7-NMP-2012-SMALL-6-310637) and the UK Engineering and Physical Sciences Research Council (EPSRC) (Grant No. EP/I001514/1), funding the Material Interface with Biology (MIB) consortium (R.K., M.B.). We thank Charlotte Boig for support with sample preparation, Dr. Cornelia Vacar (FEI) for helpful discussions on tomogram segmentations and Dr. Teresa Roncal-Herrero for support with STEM imaging (R.K., N.R.). M.B. acknowledges support from the 4D LABS shared research facility, which is supported by the Canada Foundation for Innovation (CFI), British Columbia Knowledge Development Fund (BCKDF), Western Economic Diversification Canada, and Simon Fraser University. M.M.S. acknowledges funding support from a Wellcome Trust Senior Investigator Award (098411/Z/12/Z) for the funding of N.R. N.R. gratefully acknowledges support from the Value-In-People Award from the Wellcome Trust Institutional Strategic Support Fund (097816/Z/11/A). The authors are grateful to Dr. Joseph O.P. Orgel (Illinois Institute of Technology, Chicago, IL, USA), Dr. Oleg Smirnov (Petersburg Nuclear Physics

Institute, Gatchina, Russia), Dr. Steve Weiner (Weizmann Institute of Science, Rehovot, Israel), and Dr. Marc D. McKee (McGill University, Montreal, Quebec, Canada) for critical reading of this manuscript. Also, the authors wish to thank the direct-care teams at Charing Cross Hospital for consenting patients and collecting tissue samples. The authors further thank the patients who agreed to donate tissue for research, and the Imperial College Healthcare National Health Service (NHS) staff, Dr. Geraldine A. Thomas and Imperial College Tissue Bank staff who helped with the collection of the samples, and Dr. Richard L. Abel (Imperial College London) for sharing the samples with the authors. The Imperial College NHS Tissue Bank is funded by the National Institute for Health Research - Biomedical Research Centres (NIHR-BRC), UK. Data are available online at DOI: xxyy [the data will be made available upon acceptance]